



Dynamical Models for the Sculptor Dwarf Spheroidal in a Λ CDM Universe

Louis E. Strigari¹, Carlos S. Frenk², and Simon D. M. White³

¹ Mitchell Institute for Fundamental Physics and Astronomy, Department of Physics and Astronomy, Texas A & M University, College Station, TX 77843, USA

² Institute for Computational Cosmology, Department of Physics, University of Durham, South Road, Durham DH1 3LE, UK

³ Max-Planck-Institut für Astrophysik, Karl-Schwarzschild-Straße 1, D-85740 Garching bei München, Germany

Received 2016 November 10; revised 2017 January 22; accepted 2017 January 24; published 2017 March 31

Abstract

The Sculptor dwarf spheroidal galaxy appears to contain two distinct stellar populations of differing metallicity. Several authors have argued that in order for these two populations to reside in the same gravitational potential, the dark matter halo must have a core similar to that observed in the stellar count profile. This would exclude cuspy Navarro–Frenk–White (NFW) density profiles of the kind predicted for halos and subhalos by dark matter-only simulations of the Λ CDM cosmological model. We present a new theoretical framework to analyze observations of stellar count and velocity in a self-consistent manner based on separable models, $f(E, J) = g(J)h(E)$, for the distribution function of an equilibrium spherical system. We use this machinery to analyze available photometric and kinematic data for the two stellar populations in Sculptor. We find, contrary to some previous claims, that the data are consistent with populations in equilibrium within an NFW dark matter potential with structural parameters in the range expected in Λ CDM; we find no statistical preference for a potential with a core. Our models allow a maximum circular velocity for Sculptor between 20 and 35 km s⁻¹. We discuss why some previous authors came to a different conclusion.

Key words: galaxies: kinematics and dynamics

1. Introduction

Λ CDM has emerged as the standard model of cosmic structure largely because of its successful predictions for the temperature anisotropies of the cosmic microwave background radiation, the power spectrum of the large-scale distribution of galaxies, the structure of the main body of the halos of galaxies and galaxy clusters, as inferred from weak gravitational lensing, and the broad features of the galaxy formation process (see Frenk & White 2012 for a review). However, the adequacy of the model remains controversial in the well observed inner regions of galaxies where the distribution of dark matter is strongly nonlinear (e.g., Walker & Peñarrubia 2011; Newman et al. 2013). Disagreements on these scales are particularly interesting because they could provide clues to the nature of the dark matter (e.g., Lovell et al. 2012; Peter et al. 2013; Shao et al. 2013; Zavala et al. 2013).

A robust prediction of Λ CDM is that, in the absence of baryonic effects, the spherically averaged radial density profiles of dark matter halos of all masses should approximately follow a universal form, the Navarro–Frenk–White (NFW) profile (Navarro et al. 1996, 1997), which diverges as r^{-1} toward the center. In galactic halos, baryonic effects associated with the formation of the galaxy could, in principle, flatten this central cusp through explosive events produced by supernovae, as proposed by Navarro et al. (1996) and seen more recently in a number of simulations of galaxy formation (see Pontzen & Governato 2014 for a review). Energetic arguments suggest that such processes—if they do indeed occur in nature—should be ineffective in dwarf galaxies of stellar mass below 10^6 or $10^7 M_{\odot}$, which would then retain their NFW dark matter cusps (Peñarrubia et al. 2012). Although difficult to study because of their intrinsic faintness, the dwarf galaxies with the lowest mass are thus promising sites for testing Λ CDM in the strongly nonlinear regime and learning about the identity of the dark matter and the effects of baryonic processes.

The most direct way to study the central density structure of a gas-poor galaxy is by fitting an equilibrium stellar dynamical model to a large sample of stars that have high-resolution spectroscopy and good photometry. In recent years, data of the required quality have been obtained for a number of nearby dwarf spheroidal galaxies (dSphs) around the Milky Way (Simon & Geha 2007; Walker et al. 2009) and M31 (Tollerud et al. 2012). Simple dynamical analyses based on spherical symmetry and the Jeans equations suffer from degeneracies that preclude an unambiguous determination of the dark matter potential (Strigari 2013; Walker 2013). Thus, data for several dSphs have been shown to be equally consistent with flat central profiles (cores) (Gilmore et al. 2007) or with NFW cusps (Strigari et al. 2010; Jarrel & Gebhardt 2013). In some cases, one can hope to break degeneracies by considering higher moments of the line-of-sight velocity distribution (Richardson & Fairbairn 2014).

Sculptor, a dSph of stellar mass $\sim 10^7 M_{\odot}$ located ~ 80 kpc from the Galactic Center (Lianou & Cole 2013), is a particularly interesting case. Modeling using a variety of techniques, but treating the available stellar data as sampled from a single stellar population and assuming spherical symmetry, has shown that the kinematic data are consistent with an NFW halo potential, but also allow a core (Strigari et al. 2010; Breddels et al. 2013; Richardson & Fairbairn 2014). These studies suggest a dark matter halo mass of $\simeq 10^9 M_{\odot}$ for Sculptor though with rather large uncertainties (Łokas 2009; Strigari et al. 2010; Breddels et al. 2013).

The data for Sculptor are of sufficient quality that two distinct stellar populations of differing metallicity can be identified: a centrally concentrated metal-rich (MR) population and a more extended metal-poor (MP) population (Battaglia et al. 2008, B08). The presence of two populations makes it possible to carry out more refined dynamical analyses. Thus, applying the Jeans equations to each population separately, B08 showed that their data could be fit by a model in which the

orbital distribution of each population is isotropic near the center and becomes radially biased in the outer regions. They found a best fit for a model potential with a core, but also found the data to be consistent with an NFW potential. Using Michie–King models for the stellar distribution function, Amorisco & Evans (2012) also found that while an NFW model provides an acceptable χ^2 fit to the data, models with a core seem to be preferred. On the other hand, applying the projected virial theorem, Agnello & Evans (2012) concluded that it is not possible to fit both the MR and the MP populations with a single NFW model.

An independent dynamical analysis of Sculptor using a larger sample of stars was carried out by Walker & Peñarrubia (2011, WP11). Rather than simply separating the observed stars into two populations according to their estimated metallicity, they devised a statistical method that fits the full data set simultaneously with two Plummer-profile populations of constant velocity dispersion and differing metallicity, together with a contaminating Galactic component. They then inserted the half-light radius and velocity dispersion estimated for each population into the mass estimator proposed by Walker et al. (2009). This allowed them to infer the mass contained within each half-light radius and thus the slope of the density profile between the two half-light radii. They concluded that the slope is flatter than predicted for an NFW profile at the 99% confidence level (c.l.).

In this study we carry out a new analysis of Sculptor in an attempt to clarify the conflicting claims in the literature. The specific statistical question we ask is whether the kinematic and photometric data for this galaxy exclude potentials of the type predicted by Λ CDM. We re-examine both the B08 and WP11 data sets from a different theoretical perspective and discuss how they compare. There are both similarities and differences between our analysis and those that have been undertaken previously. Like B08 and Amorisco & Evans (2012), but unlike Agnello & Evans (2012) and WP11, we exploit the full information contained within the line-of-sight velocity dispersion and photometry profiles. Like Amorisco & Evans (2012), but unlike B08, we build models based on distribution functions. Our analysis differs from that of Amorisco & Evans (2012) primarily in that we use a more flexible form for the distribution function, which allows a wider range of energy distributions and velocity anisotropies for the stars.

We conclude, in agreement with B08 and Amorisco & Evans (2012), that NFW potentials are *not* excluded by the B08 data. For our more general models the constraints used by Agnello & Evans (2012) are also no longer sufficient to exclude NFW potentials. Indeed, the implied peak circular velocity of the Sculptor dark matter halo and its concentration are consistent with the values predicted from Λ CDM simulations. While an NFW potential gives an acceptable fit to the Sculptor data, our analysis cannot exclude potentials with a core; indeed, we find below that a potential of the form proposed by Burkert (1995) provides a slightly (though not significantly) better fit to the B08 data than an NFW profile. We find similar conclusions when we apply our analysis directly to the WP11 data. Thus, our discrepant conclusions reflect differences in analysis methods rather than in observational data sets.

This paper is organized as follows. In Section 2 we introduce our model for the stellar distribution function. In Section 3 we briefly discuss our methodology for fitting the theoretical model to the data. In Section 4 we present our results, and in

Section 5 we compare them to previous studies, highlighting discrepancies where they exist.

2. Models

In this section we introduce the dynamical models we use to interpret the observed stellar populations in Sculptor. We assume each population to be spherically symmetric and to be in dynamical equilibrium within a static and spherically symmetric potential well. These are strong assumptions and should be treated as approximations. The observed stellar distribution is clearly noncircular on the sky, and Sculptor orbits within the potential of the Milky Way, so the effective potential seen by its stars is time-varying. Some aspects of the effects of flattened potentials on the dynamical analysis of dSph data are considered by Laporte et al. (2013).

2.1. Dark Matter

For the total mass density profile of the system we adopt two standard models. First, an NFW model,

$$\rho(r) = \frac{\rho_s}{x(1+x)^2}, \quad (1)$$

with corresponding gravitational potential

$$\Phi(r) = \Phi_s \left[1 - \frac{\ln(1+x)}{x} \right], \quad (2)$$

where we define $\Phi_s = 4\pi G \rho_s r_s^2$ and $x = r/r_s$. This simple model is determined by just two scale parameters—the characteristic radius r_s and the characteristic density ρ_s . Note that we define the potential to be zero at the center of the system and to be Φ_s at infinity. NFW models are often parameterized in terms of the maximum circular velocity, V_{\max} , and the radius, r_{\max} , at which this is attained. These are related to r_s and Φ_s through

$$r_{\max} = 2.16 r_s; \quad V_{\max} = 0.465 \sqrt{\Phi_s}. \quad (3)$$

Our second model is the cored profile proposed by Burkert (1995),

$$\rho(r) = \frac{\rho_b}{(1+x_b)(1+x_b^2)}, \quad (4)$$

where here $x_b = r/r_b$. This profile also has two parameters—the central density ρ_b and the scale radius r_b , and we define $\Phi_b = 4\pi G \rho_b r_b^2$. The corresponding gravitational potential is

$$\frac{\Phi(r)}{\Phi_b} = \left(1 - \frac{1}{x_b} \right) \frac{\ln(x_b^2 + 1)}{4} + \left(1 + \frac{1}{x_b} \right) \left(\frac{\tan^{-1}(x_b)}{2} - \frac{\ln(x_b + 1)}{2} \right). \quad (5)$$

As for the NFW case, we define the potential to be zero at the center of the system. With these definitions, as $r \rightarrow \infty$ we have $\Phi \rightarrow \pi \Phi_b / 4$. For the Burkert model, the maximum of the circular velocity curve and the radius at which it is attained are related to the other parameters through

$$r_{\max} = 3.245 r_b; \quad V_{\max} = 0.602 \sqrt{\Phi_b}. \quad (6)$$

2.2. Stellar Distribution Function

We define the specific energy and specific angular momentum of a star as $E = v^2/2 + \Phi(r)$ and $J = vr \sin \theta$, respectively, where v is the modulus of the velocity vector and θ is the angle between this vector and the star's position vector relative to the center of the system. Given a static and spherically symmetric gravitational potential well, any positive-definite function $f(E, J)$ corresponds to the phase-space distribution function of some stable, dynamically mixed, and spherically symmetric equilibrium for a stellar population. In this paper we will consider only models in which the dependence on E and J is separable,

$$f(E, J) = g(J)h(E), \quad (7)$$

with both $g(J)$ and $h(E)$ positive-definite and given by simple parametric forms. It would be easy to build more general, nonseparable models as a superposition of several individually separable components, but we will not pursue this further here.

The stellar density profile and the radial and tangential stellar velocity dispersion profiles of such models are given by

$$\rho_*(r) = 2\pi \int_0^\pi d\theta \sin \theta \int_0^{v_{\text{lim}}} dv v^2 g(J) h(E) \quad (8)$$

$$\rho_* \sigma_r^2(r) = 2\pi \int_0^\pi d\theta \cos^2 \theta \sin \theta \int_0^{v_{\text{lim}}} dv v^4 g(J) h(E) \quad (9)$$

$$\rho_* \sigma_t^2(r) = \pi \int_0^\pi d\theta \sin^2 \theta \sin \theta \int_0^{v_{\text{lim}}} dv v^4 g(J) h(E) \quad (10)$$

where $v_{\text{lim}} = \sqrt{2[\Phi_{\text{lim}} - \Phi(r)]}$ (we explicitly define Φ_{lim} below in Equation (18)). Note that with the definition we are using here, the total velocity dispersion at radius r is

$$\sigma_{\text{tot}}^2(r) = \sigma_r^2(r) + 2\sigma_t^2(r). \quad (11)$$

Equations (8)–(10) can be combined to give the projected stellar density profile and stellar line-of-sight velocity dispersion profile at a fixed projected distance R :

$$I_*(R) = 2 \int_0^\infty \rho_*(r) dz, \quad (12)$$

$$I_*(R) \sigma_{\text{los}}^2(R) = 2 \int_0^\infty \rho_*(r) \frac{z^2 \sigma_r^2 + R^2 \sigma_t^2}{z^2 + R^2} dz, \quad (13)$$

where $r^2 = z^2 + R^2$.

A particularly interesting and simple case occurs when the angular momentum dependence is taken to be a power law,

$$g(J) = J^b, \quad (14)$$

where $b > -2$ is a constant. For this assumption, the integrals over v and θ separate in Equations (8)–(10), and the ratio of the two velocity dispersions is independent both of r and of $h(E)$. The lower limit on b is required for the θ integrals to converge for small θ . For this choice of $g(J)$ the orbital anisotropy of the stellar population model, usually parameterized as

$$\beta(r) = 1 - \sigma_t^2(r)/\sigma_r^2(r), \quad (15)$$

is independent of radius and depends on b alone, $\beta = -b/2$. For an isotropic velocity distribution, $\beta = b = 0$. For near-radial orbits β is close to unity and b approaches its lower limit of -2 , while for near-circular orbits b is very large and positive while β is very large and negative.

In this paper we will investigate models where the orbital anisotropy varies with radius, and we therefore need a more general form for $g(J)$. We consider the function

$$g(J) = \left[\left(\frac{J}{J_\beta} \right)^{\frac{b_0}{\alpha}} + \left(\frac{J}{J_\beta} \right)^{\frac{b_1}{\alpha}} \right]^\alpha, \quad (16)$$

which interpolates between a power law of index b_0 at $J \ll J_\beta$ and a power law of index b_1 at $J \gg J_\beta$. The parameter α controls the rapidity of the transition between the two regimes at the characteristic scale, J_β , which corresponds to a radius of order $r_\beta = J_\beta/\Phi_\infty^{1/2}$, where $\Phi_\infty = \Phi_s$ for NFW and $\Phi_\infty = \pi\Phi_b/4$ for the Burkert case. In addition, α is required to be positive for $b_1 > b_0$ and to be negative in the opposite case.

For simplicity when comparing with the Sculptor data, we prefer in this paper to use a function with fewer free parameters and to assume that the velocity distribution is isotropic near the center, as seems plausible on general theoretical grounds. We therefore set $|\alpha| = 1$ and $b_0 = 0$, resulting in the simpler expression

$$g(J) = \begin{cases} [1 + (J/J_\beta)^{-b}]^{-1}, & \text{for } b \leq 0 \\ 1 + (J/J_\beta)^b, & \text{for } b > 0. \end{cases} \quad (17)$$

The upper and lower cases here correspond to radially and tangentially biased orbits for large angular momenta, respectively. Both produce isotropy for small angular momenta and so also at small radii. This simplified model retains only two parameters— J_β , which sets the extent of the inner isotropic region, and b , which determines the velocity anisotropy for large angular momenta.

For the energy distribution, $h(E)$, we have found the following form to be sufficiently general for our purposes:

$$h(E) = \begin{cases} NE^a (E^q + E_c^q)^{d/q} (\Phi_{\text{lim}} - E)^e & \text{for } E < \Phi_{\text{lim}} \\ 0 & \text{for } E \geq \Phi_{\text{lim}}, \end{cases} \quad (18)$$

where the restriction $\Phi_{\text{lim}} \leq \Phi_\infty$ is required because orbits with $E \geq \Phi_\infty$ are unbound. The normalization, N , in this expression sets the amplitude of the stellar density profile, while the exponent a determines the behavior at small energies, hence as $r \rightarrow 0$. Comparison with the simple scale-free distribution functions explored by White (1981) shows that at sufficiently small radii (where $\Phi \ll \Phi_\infty$, $E \ll E_c$, and $J \ll J_\beta$) Equations (2), (16), and (18) imply a power-law stellar density profile, $\rho_* \propto r^{-\gamma}$, where

$$\gamma = \begin{cases} -a - 3(b_0 + 1)/2, & \text{for } 2a + b_0 < -3 \text{ in NFW} \\ -2(a + b_0) - 3, & \text{for } 2a + b_0 < -3 \text{ in Burkert} \\ -b_0, & \text{for } 2a + b_0 > -3. \end{cases} \quad (19)$$

When $2a + b_0 < -3$, the density in the innermost regions is dominated by stars on orbits that are confined to those regions, while in the contrary case it is dominated by stars on orbits that extend well beyond them. Our model for $h(E)$ thus produces a central cusp in the stellar density profile when Equation (19) gives $\gamma > 0$.

At somewhat larger energies, $E > E_c$ (hence at radii larger than r_c , where $\Phi(r_c) = E_c$) the density profile steepens to a new slope, γ' , which is given by Equation (19) with a replaced by $a + d$ where we assume $d < 0$. The rapidity of the transition around r_c is controlled by the parameter $q > 0$. The final factor in Equation (18) allows for truncation of the stellar density at a radius r_{lim} defined by $\Phi(r_{\text{lim}}) = \Phi_{\text{lim}}$, which is directly analogous to the “tidal radius” in the classic King models for globular clusters (King 1966). The shape of this cutoff in the profile can be adjusted using the final parameter, e . A special case arises when $\Phi_{\text{lim}} = \Phi_{\infty}$. Then $r_{\text{lim}} \rightarrow \infty$ and the density profile at large radii becomes a power law of slope $\gamma'' = e + 3/2 - b_1/2$ (or $\gamma'' = e + 3/2 - b/2$ for the simpler case of Equation (17)).

As a final remark, we note that when $\Phi_{\text{lim}} < \Phi_{\infty}$, the constraint $E < \Phi_{\text{lim}}$ forces stellar velocities and hence stellar angular momenta to be small as $r \rightarrow r_{\text{lim}}$. The anisotropy in this region is thus determined by the form of $g(J)$ for small rather than large J , with the result that $\beta = -b_0/2$ rather than $-b_1/2$ (i.e., the distribution becomes isotropic again as $r \rightarrow r_{\text{lim}}$ if the simpler parameterization of Equation (17) is used). This complication does not arise when $\Phi_{\text{lim}} = \Phi_{\infty}$, in which case β is indeed equal to $-b_1/2$ at large radii ($-b/2$ for the simpler model of Equation (17)).

3. Data Analysis

In this section we briefly detail the Bayesian analysis methods that we will apply to the data sets described in the following sections.

For a single stellar population, the model of Equations (7), (17), and (18) is a function of nine parameters, $\{N, a, d, q, E_c, \Phi_{\text{lim}}, e, b, J_{\beta}\}$. Including the two parameters that describe the NFW potential, Equation (2), a fit to an individual stellar population has 11 free parameters, whereas a *joint* fit to both populations (each of which has independent distribution function parameters) has a total of 20 free parameters.

We use our theoretical model to fit to the binned velocity dispersion data. We define the quantities

$$\chi_{I,p}^2 = \sum_{i=1}^{n_{p,I}} \frac{[I_*(R_i) - I_p(R_i)]^2}{\delta_{p,i}^2}, \quad (20)$$

$$\chi_{\sigma,p}^2 = \sum_{i=1}^{n_{p,\sigma}} \frac{[\sigma_{\text{los}}(R_i) - \sigma_p(R_i)]^2}{\epsilon_{p,i}^2}, \quad (21)$$

where the subscript p denotes a specific population, either MR or MP. Additionally $n_{p,I}$ is the number of data points in the photometric profile of a population, and $n_{p,\sigma}$ the number of data points in the velocity dispersion profile of a population, both of which are measured at projected distance R_i . The associated measurement uncertainties are $\delta_{p,i}$ and $\epsilon_{p,i}$. Using these quantities we define a full likelihood function of the form

$$-2 \ln \mathcal{L} = \chi_{\text{total}}^2 + \text{const}, \quad (22)$$

where

$$\chi_{\text{total}}^2 = \chi_{I,\text{MR}}^2 + \chi_{\sigma,\text{MR}}^2 + \chi_{I,\text{MP}}^2 + \chi_{\sigma,\text{MP}}^2. \quad (23)$$

The constant in Equation (22) depends on the uncertainties of the photometric and velocity dispersion measurements but does not depend on the distribution function model.

We employ a Markov chain Monte Carlo (MCMC) algorithm that is an adapted version of the CosmoMC code (Lewis & Bridle 2002). From this algorithm we can extract two important quantities: (i) the maximum value of the likelihood, \mathcal{L}_{max} , which corresponds to a minimum value of χ_{total}^2 and to the “best fit” set of parameters from a given chain, and (ii) the posterior probability distribution for each model parameter. For scans of a large and complex theoretical parameter space, MCMC algorithms are not necessarily effective at finding the true value of \mathcal{L}_{max} , so it is important to determine whether the estimated value of \mathcal{L}_{max} corresponds to a set of theoretical parameters that provide a statistically good fit to the data. We thus run several chains from different starting points in the theoretical parameter space to ensure that the chains find similar values of \mathcal{L}_{max} and are thus not burning in at local maxima in the likelihood. For all models below, we find that our maximum likelihood values are robust.

The fact that we are marginalizing over up to 20 parameters also means that we must test that the posterior probability distributions for the model parameters have appropriately converged. We test for convergence of the posterior probability distributions in a standard manner by estimating the variance of a parameter as a weighted sum of the within-chain and between-chain variances (Gelman & Rubin 1992).

4. Results

B08 obtained spectroscopy for 470 stars in Sculptor, from which they measured line-of-sight velocities and metallicities derived from the calcium triplet lines. They identified two distinct populations with different metallicities, spatial distributions, and kinematics: an MR population, defined to have $[\text{Fe}/\text{H}] > -1.5$, and an MP population, defined to have $[\text{Fe}/\text{H}] < -1.7$. This clean separation and the large radial coverage of the two populations make this an attractive sample to analyze using our distribution function model described in Section 2. We fit our distribution function model to the photometric and velocity dispersion profiles reported by B08 for each population by performing a likelihood analysis using the MCMC technique, as described in Section 3. Note that the photometric profiles are obtained from a different and much larger population of stars than the velocity dispersion profiles.

Since the stellar distribution of Sculptor is elongated on the sky, B08 give the surface brightness profile of each population as a function of an “elliptical radius,” which corresponds to the projected semimajor axis determined from the photometry (Tolstoy et al. 2004). To account for this in the context of our assumption of spherical symmetry, we take as the radial coordinate the geometric mean of the major and minor axes, which we expect to correspond best to the count profile for circular annuli. We also perform the same scaling on the B08 kinematic data. The ellipticity of Sculptor is $\epsilon = 0.3$ (Irwin & Hatzidimitriou 1995).

We fit the full stellar density and velocity dispersion profiles of the two metallicity populations to the 20-parameter model defined in Section 2, which here assumes an NFW potential, and in which the velocity anisotropy can vary with radius but is assumed to be isotropic at the center. From the MCMC chains we obtain both the maximum likelihood value and the posterior probability distribution for each model parameter. The surface density and velocity dispersion profiles for a model that has near-maximal likelihood are shown in Figure 1. The count profiles of both stellar populations exhibit well defined cores.

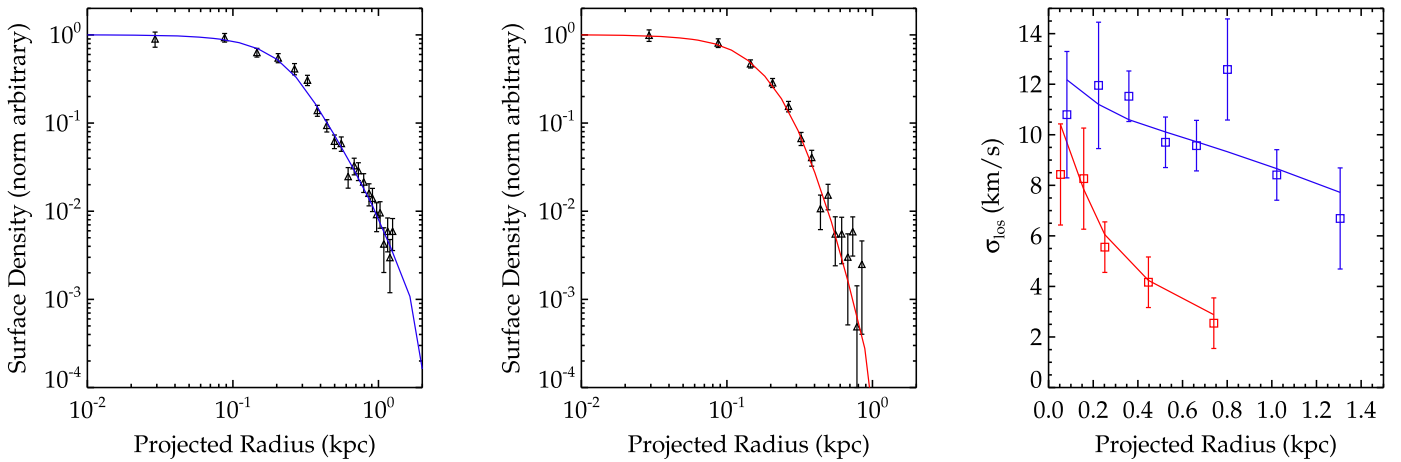


Figure 1. Best-fit model of Equations (17) and (18) to the data of Battaglia et al. (2008) for the metal-poor and metal-rich populations in Sculptor, assuming an NFW potential. The left and middle panels show the surface brightness profiles of the MP and MR populations, respectively; the right panel shows the velocity dispersion profile of the MP population (blue line at the top) and the MR population (red line at the bottom).

Table 1
An Example Distribution Function Model that Provides a Good Fit to the Sculptor Two-population Data

Population	a	d	e	E_c	Φ_{lim}	r_{lim}	b	q	J_β	V_{max}	r_{max}
MR	2.0	-5.3	2.5	0.16	0.45	1.5	-9.0	6.9	8.6×10^{-2}	21	1.5
MP	2.4	-7.9	1.1	0.17	0.60	3.0	0	8.2

Note. E_c and Φ_{lim} are in units of Φ_s , and for the MR population J_β is in units of $r_s \sqrt{\Phi_s}$; V_{max} is in km s^{-1} and r_{max} in kpc.

The MP population in this particular model is isotropic everywhere, while the MR population is isotropic in the center, has a sharp transition at a scale radius of ~ 0.2 kpc to $\beta \simeq 0.94$ over the range 0.2–1 kpc, and then transitions smoothly back to $\beta = 0$ at larger radii in order to satisfy the boundary conditions at r_{lim} . The parameters of this model are listed in Table 1.

Figure 1 shows that the data for the two metallicity populations in Sculptor are very well fit by our model, and this impression is confirmed by the values of χ^2 for the fits: 21.6 for the MP photometry (left; 23 data points), 8.8 for the MR photometry (middle; 15 data points), 8.3 for the MP kinematics (upper right; 8 data points), and 1.5 for the MR kinematics (lower right; 5 data points). Our analysis therefore demonstrates that the data are consistent with both populations residing in a single NFW potential.

Consistency with a potential of the NFW form, however, does not guarantee that the data are consistent with the predictions of the Λ CDM model. For this to be the case, the parameters of the NFW density profile must lie within the theoretically predicted range. The comparison is most easily carried out in $(V_{\text{max}}, r_{\text{max}})$ space, where the maximum circular velocity of the dark matter halo, V_{max} , and the radius, r_{max} , at which it is attained are defined in Equation (3) and are readily measured for subhalos in high-resolution Λ CDM N -body simulations of galactic halos.

The region in the $(V_{\text{max}}, r_{\text{max}})$ plane in which 90% of the subhalos in the ‘‘Aquarius’’ Λ CDM simulations of Springel et al. (2008) lie is shown by the thin lines in Figure 2. The thick lines show the 68% and 90% contours of two-dimensional joint posterior probability distributions of V_{max} and r_{max} derived from our fits to the B08 data. These contours overlap well with the theoretically predicted region, demonstrating that the kinematics of the populations in Sculptor are fully consistent with expectations in a Λ CDM universe. The range of V_{max}

allowed by our fits, $\sim(20\text{--}35) \text{ km s}^{-1}$, is significantly wider than the range estimated in some previous analyses (Boylan-Kolchin et al. 2011).

To compare the quality of our NFW fits to that obtained for a cored potential, Figure 3 presents results from a joint analysis of the two populations using a Burkert profile. In this case, we also have 20 parameters, but we replace (ρ_s, r_s) by (ρ_b, r_b) . The best-fit $V_{\text{max}}\text{--}r_{\text{max}}$ values in this figure are almost identical to those found in the NFW case, but the constraints are considerably tighter, reflecting the much more sharply defined characteristic scale of the cored potential. The total χ^2 for the best fit is 39.3 in the Burkert case, which is slightly but not significantly smaller than the value of 40.2 that we found for the best fitting NFW potential.

Given the similar quality of the fits for the two profiles, we consider the more general question of whether we can expect to distinguish them with kinematic and photometric data sets similar to those of B08. We start from distribution function parameters resembling those of our best Burkert fit to B08, and generate mock photometric and kinematic data sets with similar size and uncertainties to B08. We consider several values for the Burkert scale radius and scale density, chosen to give dispersion and count profiles similar to those observed. The largest value for the scale radius we consider is $r_b = 1$ kpc. We fit these mock data to Burkert and NFW models, comparing the best-fit χ^2 values in the two cases. Even for $r_b = 1$ kpc, we find NFW models with very similar χ^2 to the best fitting Burkert model. The latter always has parameters very close to the input values, showing our procedure to be approximately unbiased. This test implies that the B08 data samples are not large enough to be able to distinguish between Burkert and NFW potentials on the basis of count and velocity dispersion profiles. We will return to the

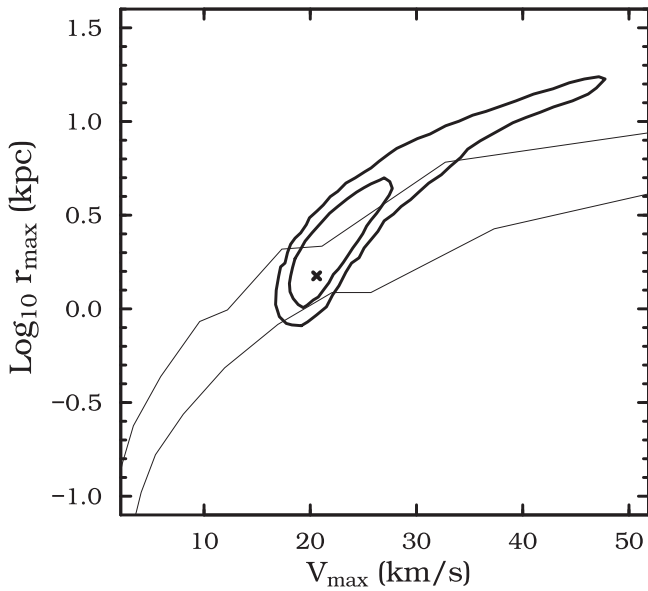


Figure 2. 68% and 90% c.l. regions in the V_{\max} - r_{\max} plane for fits of the model of Equations (17) and (18) to the two metallicity populations in Sculptor (thick lines). A cross indicates the model of Table 1. Thin lines delineate the region that contains 90% of the subhalos from the Aquarius Λ CDM simulations of galactic halos (Springel et al. 2008).

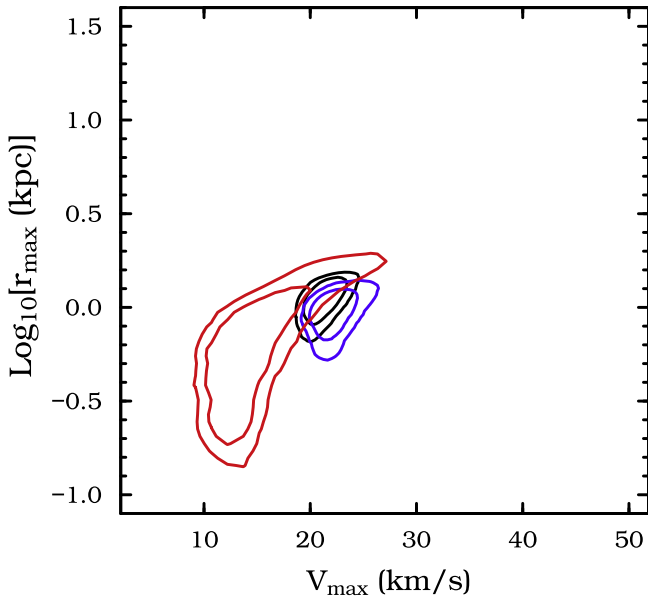


Figure 3. 68% and 90% confidence contours in the V_{\max} - r_{\max} plane for independent fits to the two metallicity populations in Sculptor assuming a Burkert profile. The red contours are obtained by fitting the 11-parameter model of Equations (17) and (18) to the B08 MR data, while the blue contours are obtained from fitting the same 11-parameter model to the B08 MP data. These contour sets can be compared with Figure 4 for the NFW profile. The black contours are the results of a joint fit to the MR and MP data as shown for the NFW profile in Figure 2.

issue of distinguishing between these two models below when discussing the WP11 data.

5. Comparison to Previous Results

Several previous studies have constrained the potential in Sculptor by splitting its stars into high- and low-metallicity

populations and requiring each separately to be in equilibrium. In this section we compare our results with these earlier analyses.

5.1. Battaglia et al. (2008)

In the first dynamical analysis to separate the two populations in Sculptor, B08 applied the Jeans equation to each population individually, fitting the star count profiles to standard forms (Plummer for the metal-rich, Sérsic for the metal-poor) and then predicting the velocity dispersion profiles for various assumed potentials and anisotropy profiles. They found that their data were consistent with both NFW and core potentials, but required radially biased orbits for both populations.

Our results largely corroborate the conclusions reached by B08. Our use of a flexible stellar distribution function removes the need to assume standard forms for the count and anisotropy profiles and ensures that the resulting model is physically realisable. As a result, our best-fit model has a smaller χ^2 than the model of B08. Like B08, we find that radially biased orbits are required at large radii for the metal-rich (although not for the metal-poor) population.

5.2. Amorisco & Evans (2012)

Of the previous studies, that of Amorisco & Evans (2012) is most similar to our own. They also assumed separable distribution functions for the two populations and fit predicted counts and velocity dispersion profiles to the data of B08. They considered both NFW potentials and pseudo-isothermal potentials with a core. Although the form they assumed for their distribution functions is considerably less flexible than our own, the resulting best fit for an NFW potential is similar to ours, shown in Figure 1, and has a χ^2 value that is clearly insufficient to exclude the model. The best fit for the core case also looks similar (compare their Figures 9 and 10). Nevertheless, its χ^2 value is sufficiently smaller that a likelihood ratio test clearly prefers it over an NFW potential.

As Amorisco & Evans (2012) note, the preference for a core potential over a cuspy one is driven in their analysis by its lower prediction for the innermost points of the count profiles, and to a lesser extent by a somewhat larger predicted difference in velocity dispersion between the two populations. With our more flexible distribution function model, the count discrepancy at small radii disappears for the NFW potential and the difference in velocity dispersions between the MP and MR populations is slightly enhanced (see Figure 1), leading to a fit of very similar quality to that found by Amorisco & Evans (2012) for their core potential. A final difference with Amorisco & Evans (2012) is that their NFW fit required a halo concentration that is lower than expected in Λ CDM. With our distribution function model, this problem has disappeared.

5.3. Agnello & Evans (2012)

Agnello & Evans (2012) applied the projected virial theorem separately to the two populations identified by B08, assuming that they reside in an NFW potential and have Plummer-law surface brightness profiles. With these assumptions, the observational data for each population imply a relation between V_{\max} and r_{\max} for its halo. They then show that the regions of the (V_{\max}, r_{\max}) plane allowed at 2σ by the MR and MP data do not overlap. They therefore conclude that no single NFW potential can accommodate both populations.

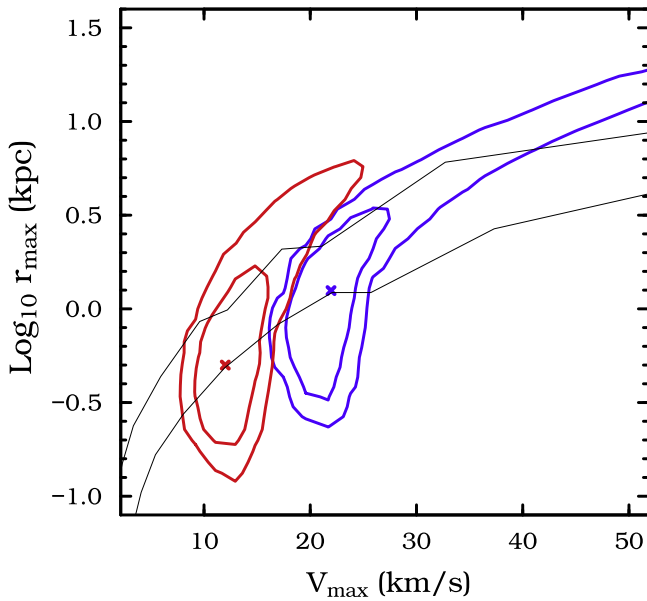


Figure 4. 68% and 90% c.l. contours in the V_{\max} - r_{\max} plane for *independent* fits to the two metallicity populations in Sculptor. The red contours are obtained from fitting the 11-parameter model of Equations (17) and (18) to the B08 MR data, while the blue contours are obtained from fitting it to the B08 MP data. Crosses in each case indicate the best-fit model.

B08 noted that the metal-poor population in Sculptor is poorly fit by a Plummer model. By applying our procedures to the MR and MP data separately, we can perform an analysis analogous to that of Agnello & Evans (2012). In Figure 4 we show the two-dimensional joint posterior probability distributions of (V_{\max}, r_{\max}) . We indeed reproduce an offset similar to that seen by Agnello & Evans (2012). However, the greater freedom afforded by our relaxation of the Plummer-law assumption, allowing instead any profile consistent with the observed counts, widens the confidence regions so that they are no longer exclusive. The two distributions are marginally consistent with each other for $V_{\max} \sim 15\text{--}25 \text{ km s}^{-1}$ and $r_{\max} \sim 1 \text{ kpc}$, which, not surprisingly, is the region also picked out by our single-potential model. We note that even though Figure 4 appears to indicate that the individual population fits are only marginally consistent with the same potential parameters, the χ^2 of the joint fit presented in the discussion of Figure 1 indicates that the two-population NFW model does indeed provide an excellent fit to the data. As before, the potential parameters are consistent with the Λ CDM predictions of Springel et al. (2008).

5.4. Walker & Peñarrubia (2011)

WP11 analyzed a sample of 1497 stars with spectroscopy, from which they derive line-of-sight velocities and an Mg index that they take as a proxy for metallicity. In practice, we are able to work with the subsample of 1307 stars for which the public online data set lists a membership probability value. WP11 use MCMC techniques to map the parameter distributions for a three-component model of these data. The metal-rich and metal-poor populations are each represented by a circularly symmetric Plummer profile, with Gaussian velocity and metallicity distributions independent of radius (note that these assumptions are not consistent with the B08 data), while the contaminating Galactic foreground is taken to be spatially uniform with broader distributions of velocity and metallicity.

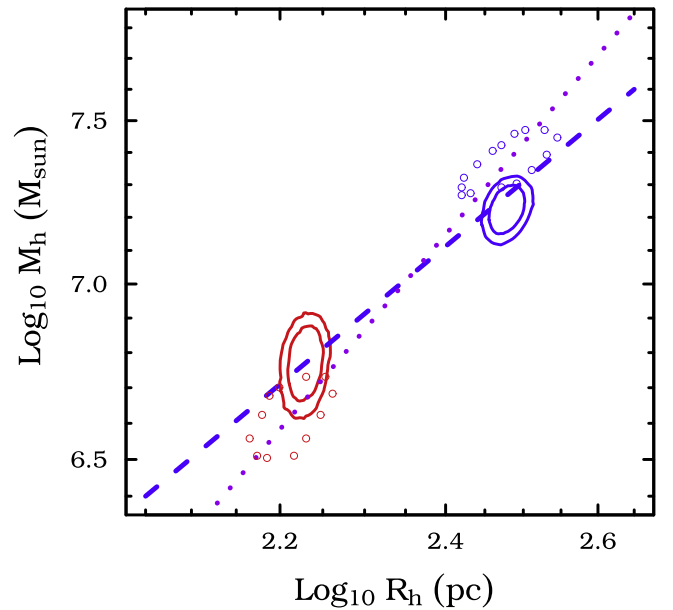


Figure 5. Constraints from WP11 and from the models of this paper in the (R_h, M_h) plane. The two straight lines and the contours traced by open circles are taken directly from Figure 10 of WP11 and indicate $M \propto r^\alpha$ with $\alpha = 2, 3$ and the 50% c.l. regions given by their MCMC analysis for the parameters of the two underlying populations. For comparison, the solid contours show 68% and 90% c.l. regions from our own MCMC chains constrained by the B08 data and assuming both populations to be in equilibrium within a single NFW potential.

They insert the half-light radius and velocity dispersion estimated by this analysis for each population into the mass estimator proposed by Walker et al. (2009):

$$M_h = M(R_h) = 2.5 \langle \sigma_{\text{los}}^2 \rangle R_h / G, \quad (24)$$

which gives the mass, M_h , inside a sphere with radius equal to the projected half-light radius, R_h , in terms of the measured velocity dispersion, σ_{los}^2 , and R_h .⁴ The derived increase in estimated mass between the two values of R_h appears too large to be consistent with an NFW profile and is close to that expected for a core of constant density. WP11 conclude that NFW is excluded at the 99% c.l.

This conclusion is incompatible with our conclusion derived above, based on the B08 data. In Figure 5 we show the results of WP11 in the (R_h, M_h) plane, together with lines corresponding to $M \propto r^\gamma$, with $\gamma = 2$ and $\gamma = 3$. Clearly, these results agree much better with the dotted line representing a core than with the dashed line representing an NFW cusp. Our MCMC analysis based on the distribution function allows us to reconstruct R_h and M_h for all models consistent with the B08 data and residing in an NFW potential. Solid red and blue contours in Figure 5 give the 68% and 90% confidence regions for the metal-rich and metal-poor populations respectively. As expected, the center points of these contours define a slightly shallower slope than the dashed line since $\gamma = 2$ only in the innermost regions of an NFW profile. The half-light radii found for the MR and MP populations in the two analyses agree well but there is an offset in the preferred M_h values, although the contours do overlap. Hence, fitting our models to the B08 data has resulted in lower velocity dispersions for the

⁴ This estimator is constructed to be only weakly sensitive to the details of the density and velocity anisotropy profiles (see also Wolf et al. 2010).

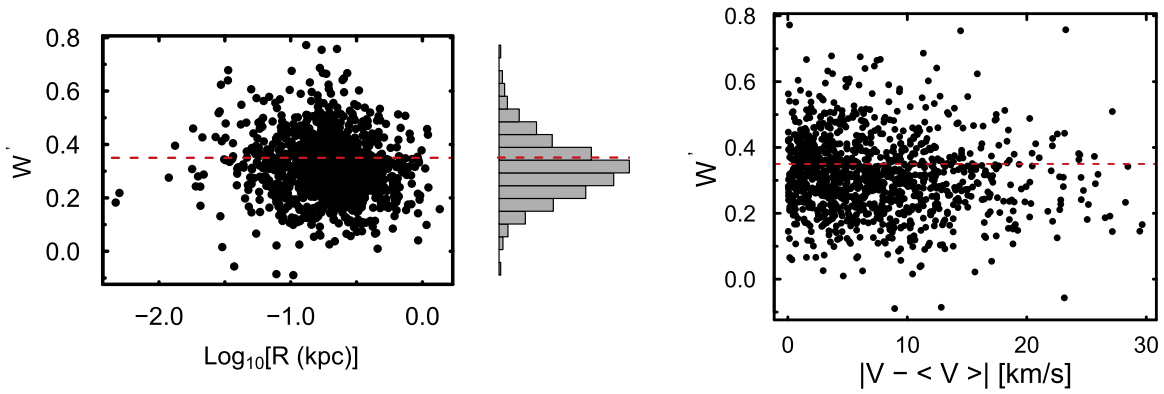


Figure 6. Reduced Mg index, W' , vs. radius (left) and velocity (right) for stars considered to be probable Sculptor members by WP11. The histogram plotted vertically (center) shows the distribution of W' for the sample as a whole. The red dashed line defines the cut that maximally separates the radial distributions of metal-rich and metal-poor populations.

MP population and higher velocity dispersions for the MR one than estimated by WP11 from their own data.

To determine whether the WP11 data favor a cored or cusped halo when analyzed using our procedures, we construct binned photometric and velocity dispersion profiles directly from the WP11 data. Figure 6 shows the metallicity as a function of both radius and velocity for the 1160 stars in the tables published by WP11 that have high-quality data and are assigned a membership probability $>99\%$. The W' distribution of the member stars is unimodal, with no obvious indication of two distinct populations. To separate the stars by metallicity into two populations with maximally distinct spatial distributions, we split them at a given value of W' in the left panel of Figure 6, and then perform a Kolmogorov–Smirnov (KS) test to determine the significance of the difference in radial distribution between the two populations. The value of W' that minimizes the KS p -value then defines the MR and MP populations with the most significantly distinct spatial distributions.

Following this procedure, we find a minimum p -value of 1.4×10^{-7} at $W' = 0.35$. This cut gives 763 MP members with $W' \leq 0.35$, and 397 MR members with $W' > 0.35$. The left panel of Figure 6 shows that, with this cut, the fraction of MR stars at large radii is noticeably smaller than for the MP stars. Including all 1307 WP11 stars with a membership probability, regardless of its value, increases the p -value by nearly two orders of magnitude, but still gives an optimal separation at about the same W' value, and with a similar ratio of MR to MP stars. For comparison, in their statistical separation, WP11 found that 53% of the Sculptor member stars belong to the underlying “true” MR population, and the remainder to the MP population.

The velocity dispersion and the photometry profiles of the two populations are shown in Figure 8. In comparison to the B08 data in Figure 1, the WP11 data cover a narrower range of radii but have higher signal-to-noise ratio for the velocity dispersion measurements. For all four profiles, we have corrected the raw numbers using the radial selection function as suggested in WP11. We find the half-light radii for the MR and MP populations to be 0.18 and 0.22 kpc, respectively. The MR half-light radius is in good agreement with that derived by WP11, while the MP half-light radius is significantly smaller than the value of 0.30 kpc derived by WP11. The velocity dispersion profile of the MR component derived from

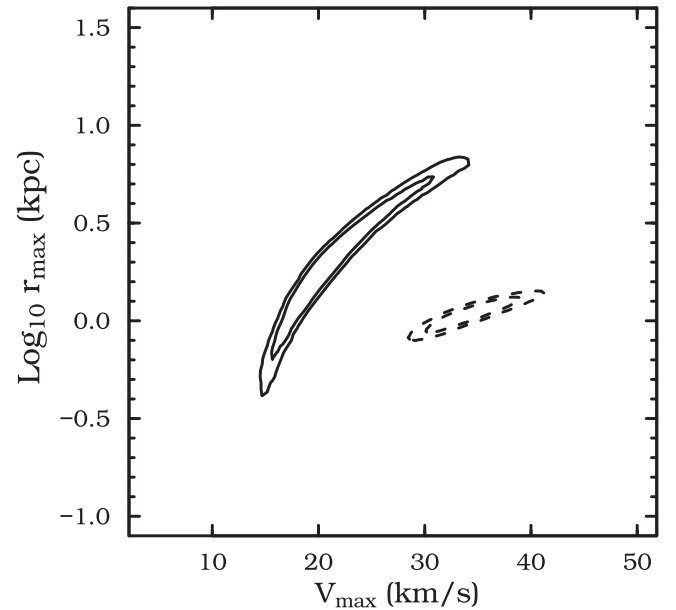


Figure 7. 68% and 90% c.l. contours in the V_{\max} – r_{\max} plane for *joint* fits to the two metallicity populations in Sculptor using the WP11 data split according to the cut in Figure 6. Solid contours are for an NFW potential and dashed are for a Burkert one.

the WP11 data does not show a steep decline at large radii of the kind seen in the B08 data.

An MCMC analysis of the WP11 data results in allowed regions in the V_{\max} – r_{\max} parameter space shown in Figure 7 for both Burkert and NFW profiles. For the NFW profile, the derived values of V_{\max} are in good agreement with the values derived from the B08 data, while for the Burkert profile the central V_{\max} is larger, peaking at $\sim 30 \text{ km s}^{-1}$. The corresponding best fitting photometry and velocity dispersion profiles are shown in Figure 8. The χ^2 for the best fitting profiles for both joint and individual fits are given in Table 2. Note that in both cases we are fitting 34 data points to a 20-parameter model. So the χ^2 values we find indicate fully acceptable fits and show a slight preference for NFW over Burkert.

We thus conclude that when analyzed with the methods of this paper the WP11 data do not favor a core over a cusp. This result is in disagreement with that of WP11, who find NFW profiles to be ruled out with $>99\%$ confidence. At this point we are unable to determine why our conclusions differ from those

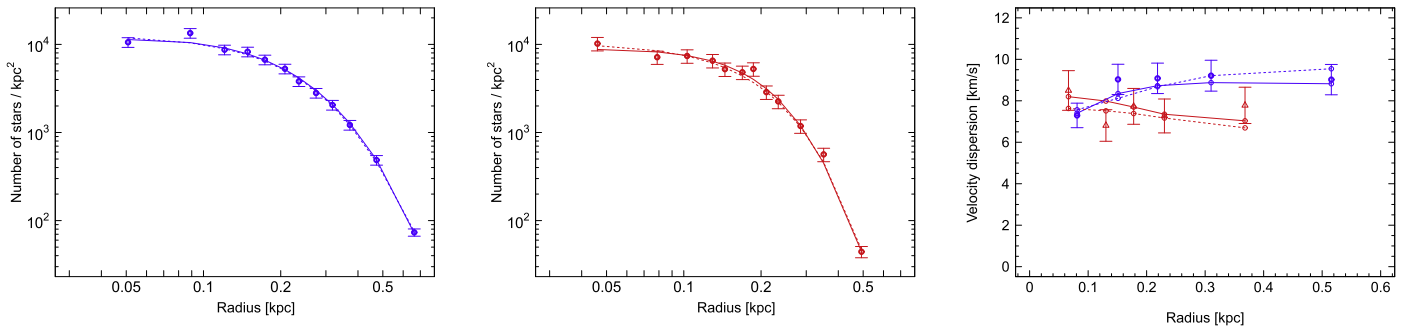


Figure 8. Results of *joint* fits to the MP (left) and MR (middle) photometry and kinematics (right), using the WP binned data. In each panel, the solid line assumes an NFW potential, and the dashed line a Burkert one.

Table 2
Total χ^2 Values for the Best Fit to the Photometry
and Kinematic Profiles using the WP11 Data

	NFW		Burkert	
	Photometry	Dispersion	Photometry	Dispersion
MR	5.5	3.9	6.0	2.8
MP	5.0	1.2	5.5	3.2

of WP11. Our dynamical analysis is based on self-consistent distribution function models with considerable flexibility, which can be exploited to obtain good simultaneous fits to the photometric and kinematic data. In contrast, WP11 use simple, Plummer-law models with constant velocity dispersion, which are inconsistent in detail with the Sculptor data. However, since these are used only to estimate the half-light radii and total velocity dispersions of the two populations, it is unclear whether this inconsistency can significantly bias their results. A second difference is that our likelihood analysis explicitly separates Sculptor stars into two populations based on the directly measured quantity W' and rejects *ab initio* the small number of stars that are not high-probability members, whereas WP11 treat W' as an indicator of the relative probability of belonging to one or other of two assumed underlying populations, and also treat background rejection probabilistically. However, at the present time it is unclear whether these differences can account for the difference in our conclusions. Figure 8 does appear to demonstrate that our model can reproduce the WP11 data very well in an NFW potential.

6. Conclusions

In this paper we have presented a new framework based on separable distribution functions to study stellar populations in equilibrium within a spherical dark matter potential well. We use it to study the two metallicity populations in the Sculptor dwarf spheroidal galaxy, and in particular to explore the controversial question of whether their properties exclude a cuspy profile of the kind expected in the Λ CDM cosmology.

The family of distribution functions we consider gives substantially more freedom than the models assumed in previous studies, and as a result it leads to a weakening of the constraints implied by the observations. Although, in the absence of any prior on the shape of the inner potential, we concur with previous studies that the Sculptor data prefer a shallower profile than NFW, we find this preference to be far too weak to exclude the cosmological prediction. Indeed, in a

χ^2 sense, we are able to find equilibrium models that are a good fit to the data sets of both B08 and WP11 within an NFW potential with parameters that are fully consistent with Λ CDM.

Since the inner structure of dwarf galaxies appears at present as one of the few significant challenges to the standard cosmological paradigm, it is unsurprising that considerable attention has been focused on measuring this structure precisely. Unfortunately, the problem is underconstrained by currently available data, given the considerable freedom inherent in the equations of stellar dynamics. The analysis in this paper, while comparatively general, still makes at least two major assumptions that are known to be incorrect: dwarf spheroidal galaxies are clearly not spherically symmetric and their orbits within the Milky Way's potential ensure that most cannot be static systems in equilibrium. Further theoretical progress will require these shortcomings to be addressed. (See Zhu et al. (2016) for a recent study of Sculptor that relaxes the assumption that the stellar distribution is spherical, while continuing to assume a spherical potential.) Further observational progress may be achieved by reducing the statistical and measurement uncertainties, and in the more distant future by increasing the phase-space coverage through measurement of internal proper motions.

We would like to thank Chervin Laporte for his critical comments on an earlier version of this work, which prompted us to develop the distribution function methods used in this paper. We also thank Matt Walker for critical and constructive comments on the paper. Much of the theoretical modeling framework for this paper was developed at the Aspen Center for Physics, which is supported by National Science Foundation grant PHY-1066293. L.E.S. acknowledges support from National Science Foundation grant PHY-1522717. This material is based upon work supported by the National Science Foundation under Grant No. CNS-0723054. C.S.F. acknowledges ERC Advanced Investigator Grant COSMIWAY and SDMW ERC Advanced Investigator Grant GALFORMOD. This work was supported in part by an STFC rolling grant to the ICC. This work used the DiRAC Data Centric system at Durham University, operated by the Institute for Computational Cosmology on behalf of the STFC DiRAC HPC Facility (www.dirac.ac.uk). This equipment was funded by BIS National E-infrastructure capital grant ST/K00042X/1, STFC capital grant ST/H008519/1, and STFC DiRAC Operations grant ST/K003267/1 and Durham University. DiRAC is part of the National E-infrastructure.

References

- Agnello, A., & Evans, N. W. 2012, *ApJL*, 754, L39
- Amorisco, N. C., & Evans, N. W. 2012, *MNRAS*, 419, 184
- Battaglia, G., Helmi, A., Tolstoy, E., et al. 2008, *ApJL*, 681, L13
- Boylan-Kolchin, M., Bullock, J. S., & Kaplinghat, M. 2011, *MNRAS*, 415, L40
- Breddels, M. A., Helmi, A., van den Bosch, R. C. E., van de Ven, G., & Battaglia, G. 2013, *MNRAS*, 433, 3173
- Burkert, A. 1995, *ApJL*, 447, L25
- Frenk, C. S., & White, S. D. M. 2012, *AnP*, 524, 507
- Gelman, S., & Rubin, D. 1992, *StaSc*, 7, 457
- Gilmore, G., Wilkinson, M. I., Wyse, R. F. G., et al. 2007, *ApJ*, 663, 948
- Irwin, M., & Hatzidimitriou, D. 1995, *MNRAS*, 277, 1354
- Jardel, J. R., & Gebhardt, K. 2013, *ApJL*, 775, L30
- King, I. R. 1966, *AJ*, 71, 64
- Laporte, C. F. P., Walker, M. G., & Peñarrubia, J. 2013, *MNRAS*, 433, L54
- Lewis, A., & Bridle, S. 2002, *Phys. Rev. D*, 66, 103511
- Lianou, S., & Cole, A. A. 2013, *A&A*, 549, A47
- Łokas, E. L. 2009, *MNRAS*, 394, L102
- Lovell, M. R., Eke, V., Frenk, C. S., et al. 2012, *MNRAS*, 420, 2318
- Navarro, J. F., Eke, V. R., & Frenk, C. S. 1996, *MNRAS*, 283, L72
- Navarro, J. F., Frenk, C. S., & White, S. D. M. 1996, *ApJ*, 462, 563
- Navarro, J. F., Frenk, C. S., & White, S. D. M. 1997, *ApJ*, 490, 493
- Newman, A. B., Treu, T., Ellis, R. S., & Sand, D. J. 2013, *ApJ*, 765, 25
- Peñarrubia, J., Pontzen, A., Walker, M. G., & Koposov, S. E. 2012, *ApJL*, 759, L42
- Peter, A. H. G., Rocha, M., Bullock, J. S., & Kaplinghat, M. 2013, *MNRAS*, 430, 105
- Pontzen, A., & Governato, F. 2014, *Natur*, 506, 171
- Richardson, T., & Fairbairn, M. 2014, *MNRAS*, 441, 1584
- Shao, S., Gao, L., Theuns, T., & Frenk, C. S. 2013, *MNRAS*, 430, 2346
- Simon, J. D., & Geha, M. 2007, *ApJ*, 670, 313
- Springel, V., Wang, J., Vogelsberger, M., et al. 2008, *MNRAS*, 391, 1685
- Strigari, L. E. 2013, *PhR*, 531, 1
- Strigari, L. E., Frenk, C. S., & White, S. D. 2010, *MNRAS*, 408, 2364
- Tollerud, E. J., Beaton, R. L., Geha, M. C., et al. 2012, *ApJ*, 752, 45
- Tolstoy, E., Irwin, M. J., Helmi, A., et al. 2004, *ApJL*, 617, L119
- Walker, M. 2013, in *Planets, Stars and Stellar Systems, Vol. 5: Galactic Structure and Stellar Populations*, ed. T. D. Oswalt & G. Gilmore (Dordrecht: Springer), 1039
- Walker, M. G., Mateo, M., & Olszewski, E. W. 2009, *AJ*, 137, 3100
- Walker, M. G., Mateo, M., Olszewski, E. W., et al. 2009, *ApJ*, 704, 1274
- Walker, M. G., & Peñarrubia, J. 2011, *ApJ*, 742, 20
- White, S. D. M. 1981, *MNRAS*, 195, 1037
- Wolf, J., Martinez, G. D., Bullock, J. S., et al. 2010, *MNRAS*, 406, 1220
- Zavala, J., Vogelsberger, M., & Walker, M. G. 2013, *MNRAS*, 431, L20
- Zhu, L., van de Ven, G., Watkins, L. L., & Posti, L. 2016, *MNRAS*, 463, 1117